minerals

MDPI

Article

Numerical Study on the Hydraulic Fracturing Pattern in the Hard Roof in Response to Mining-Induced Stress

Junchao Chen [1], Zhengzhen Qu [2], Lei Zhou [3] and Xiaopeng Su [4,*]

[1] School of Emergency Management, Xihua University, Chengdu 610039, China
[2] Department of Emergency Management of Sichuan Province, Chengdu 610047, China
[3] State Key Laboratory of Coal Mine Disaster Dynamics and Control, Chongqing University, Chongqing 400044, China
[4] School of Civil Engineering, Chongqing Jiaotong University, Chongqing 400074, China
* Correspondence: suxiaopeng@cqjtu.edu.cn

Highlights:

What are the main findings?

- The 3D stress distributions around the gob after mining are numerically calculated.

What is the implication of the main finding?

- The propagations of hydraulic fractures in different disturbed areas caused by mining-induced stress are compared.
- The influence of the geological conditions that often appear in situ in hydraulic fracturing patterns in a hard roof is examined.

Abstract: A hard roof can cause serious issues corelated with the stability of the panel including large deformation of the roadway in the gob, rock burst, coal and gas outbursts, etc. Currently, hydraulic fracturing has ever-increasingly been used to help control these above-mentioned issues in many engineering cases. This paper presents a series of numerical simulations for hydraulic fracturing with a recently developed model to examine the weakening effect of this pre-conditioning measure on a hard roof. The results show that large deflections in the principal stress direction occur above the coal seam after mining, which can be progressively enhanced as the working face continuously advances. This further could significantly affect the hydraulic fracturing pattern and result in arc-shaped fracture propagation, especially for the hydraulic fracture in stress-descending areas. The obtained results suggest that the hydraulic fracturing operation in a hard roof is preferable in the areas close to the middle of the gob where the created fractures would be deflected more. At last, sensitivity analysis shows that geological conditions have great influence on the hydraulic fracturing pattern. Among the factors analyzed in this paper, the difference between the maximum and minimum stress has the largest influence and should be fully considered. This study could provide a theoretical basis for the practical hydraulic fracturing operation in a hard roof.

Keywords: hydraulic fracturing; hard roof; numerical simulation; mining-induced stress; fracture

check for updates

Citation: Chen, J.; Qu, Z.; Zhou, L.; Su, X. Numerical Study on the Hydraulic Fracturing Pattern in the Hard Roof in Response to Mining-Induced Stress. *Minerals* **2023**, *13*, 308. https://doi.org/10.3390/min13030308

Received: 28 January 2023
Revised: 16 February 2023
Accepted: 21 February 2023
Published: 22 February 2023

Copyright: © 2023 by the authors. Licensee MDPI, Basel, Switzerland. This article is an open access article distributed under the terms and conditions of the Creative Commons Attribution (CC BY) license (https://creativecommons.org/licenses/by/4.0/).

1. Introduction

In coal mines, a hard roof refers to a roof that is located above the coal seam and could supply structural support. It is characterized by large thickness, high strength and good integrity. In China, a hard roof exists in more than 30% of coal mines [1]. After the extraction of the coal seam, the hard roof is usually exposed and suspended without collapse in the mined-out area, which could concentrate stresses and elastic energy as being deformed and gradually bent. Once the hard roof suddenly collapses, it is often accompanied by strong dynamic pressure phenomena such as large deformation of the roadway in the gob, rock

burst, coal and gas outbursts, etc. [2–6]. Such cases are more serious at large mining depths due to the larger overburden stresses. Data statistics show that the accidents caused by a hard roof account for approximately 70–80% of the total mine accidents every year [7,8]. Clearly, the hard roof has become a major threat to the safety and efficient production of coal mines. It is therefore necessary that pre-conditioning measures be evolved to tackle the strong damaging effects caused by the hard roof.

At present, approaches such as support, water-infusion softening, blasting and hydraulic fracturing are adopted for weakening the hard roof. However, support cannot fundamentally solve the problem induced by the tight roof and coal pillar support often leads to huge resource waste; water-infusion softening is limited to its effective range and also cannot decrease the working face pressure on a large scale and blasting often results in serious underground air pollution and coal and gas outbursts. In comparison with these approaches, hydraulic fracturing has the advantages of improved control of the fracture geometry through the shadow stress effect and directional fracturing. Hydraulic fracturing technology was first successfully applied in the field of oil and gas in 1949 [9], and now it has been gradually extended to the application of the coal mine. In addition to pressure relief and permeability enhancement of the coal seam [10–14], it is also increasingly applied to solve the problem of the hard roof [15–24]. In engineering practice, hydraulic fracturing boreholes are drilled from the ground surface/subsurface excavations into the target rock strata and then water is artificially injected to create complex hydraulic fractures. That is, the objective of hydraulic fracturing in the hard roof is to make the hard roof blocky so that it can collapse with desirable fragmentation sizes as the working face advances. Engineering practices confirm that hydraulic fracturing could bring about stress relief in the hard roof and realize better control in the deformation of the roadway in the gob. For instance, Shimada et al. [25] realized the better control of periodic weighting and wind blast with the application of hydraulic fracturing and moistening technique. Hays [26] applied hydraulic fracturing to successfully achieve consistent desirable falls and then avoided the potential sudden caving with the longwall coal panel mining. Huang et al. [27] succeeded in increasing the cavability of top coal during longwall top coal caving using hydraulic fracturing. A field case study has shown that hydraulic fracturing in the main roof above the coal seam could significantly reduce abutment stresses [28]. In essence, the key of this technology is to control the initiation and propagation of created hydraulic fractures so as to cut rock stratum accurately and directionally. The existing knowledge has suggested that the orientation of hydraulic fractures be positively corelated with the stress state imposed to the target stratum, and that it often propagates along the direction perpendicular to the minimum principal stress [29–31]. In engineering practice, hydraulic fracturing operations are often carried out based on this principle to create hydraulic fractures. Nevertheless, it is found that in most practical cases, the pre-conditioning hydraulic fracture patterns are not effective and desirable for weakening a blocky hard roof that can collapse under gravity. The main reason for such cases is that hydraulic fracturing operations are often designed based on the stress states in the target rock stratum before mining; however, after mining, the original stress states are strongly disturbed by the mined-out area [32–34], which further results in some undesirable deflections of hydraulic fractures. Uncontrollable fracture complexity is a huge threat to mining safety and also to high efficiency exploitation. Hence, a better understanding of the mechanism for the hydraulic fracturing pattern in response to mining-induced stresses is essential for achieving good hard roof control. However, limited studies have been directly conducted on this issue in coal mining practice.

Up to now, numerous studies on hydraulic fracturing patterns in the hard roof have been experimentally and numerically performed. Xu et al. [35] built a sheet model with four fixed sides and found that hard roof square breaking caused the mine pressure to be the greatest. Li [36] used physical models with the AE monitoring technique to investigate fracture characteristics in the hard roof and discovered that when a hard roof fractured, lots of energy was released; meanwhile, the AE warning increased dramatically. In fact, laboratory tests often need to build similar physical models, which is time-consuming,

costly, laborious and unrepeatable. This is particularly true for 3D cases. Numerical simulation, which can reproduce the engineering geological conditions in a more real way and is also more convenient for establishing the model, has gradually become the main method to study the propagation and evolution of the hydraulic fracturing pattern. He et al. [29] concluded that the re-orientation geometry of the hydraulic fracture was affected by both the differential stress between σ_2 and σ_3 and between σ_1 and σ_3. Xia et al. [37] studied the weakening effects of hydraulic fracturing on the hard roof under the influence of a stress arch. The results showed that the principal stress directions deflected after mining, which further led to the inclination in the hydraulic fracture propagation path. However, these above-mentioned simulations are limited to 2D cases, which are strictly not the same as the actual 3D in situ cases and therefore this limits the engineering application of relevant research results to a certain extent. To design an effective strategy for creating a hydraulic fracturing pattern with controllable orientation in each geological condition, comprehensive research in 3D cases is required and critical. In addition, He et al. [38] confirmed that hydraulic fractures were influenced by various factors such as the differential stress, the minimum principal stress direction, etc. Therefore, the sensitivity of the hydraulic fracturing pattern to these factors is significant and must be well understood.

In this paper, the hydraulic fracturing patterns in the hard roof in response to the mining-induced stresses are numerically studied with a finite difference code to improve the understanding of the hydraulic fracturing pre-conditioning method. The major relevant theory details of the used models can be found in [39,40]. A brief description for these models is given in this paper. First, the mining-induced stress fields around the coal seam are identified for different mining distances. Second, the spatial morphologies of hydraulic fractures in the hard roof under different mining stresses are simulated. Finally, sensitivity analysis is conducted to examine the effect of various geological factors on the hydraulic fracturing pattern. The novelty in this paper is in clarifying how many hydraulic fracture defects there are in response to the complicated mining-induced stresses on 3D scales. The obtained results could provide a helpful guide for obtaining desirable fracture complexity by means of hydraulic fracturing.

2. Theoretical Background

2.1. Constitutive Models for Longwall Mining

Based on the equivalent continuum theory, it is assumed that rock deformation is comprised of two parts, namely rock matrix (rock element without fracture) and fracture (rock element with fracture), which are described as follows.

2.1.1. The Models for Rock Element without Fracture

The most widely used Mohr–Coulomb criterion in the rock engineering field is adopted for determining the yield of the rock matrix, which is given as follows:

$$\begin{Bmatrix} F_s \\ F_t \end{Bmatrix} = \begin{Bmatrix} \sigma_1 - N_\varphi \sigma_3 + 2c\sqrt{N_\varphi} \\ \sigma_3 - \sigma_t \end{Bmatrix} \tag{1}$$

where σ_1 and σ_3 are the maximum and minimum principal stresses, [Pa]; φ is the internal friction angle, [°], and σ_t is the rock tensile strength, [Pa]. $N_\varphi = (1 + sin\varphi)/(1 - sin\varphi)$. Once rock matrixes are yielded, the plastic strain increment is determined by the associated flow rule. Herein, we use the second strain deviator and maximum tensile strain to evaluate the shear and tensile plastic strain, respectively. They read [41] as follows:

$$\begin{Bmatrix} \varepsilon_s \\ \varepsilon_t \end{Bmatrix} = \begin{Bmatrix} \sqrt{\frac{(\varepsilon_1^p - \varepsilon_2^p)^2 + (\varepsilon_2^p - \varepsilon_3^p)^2 + (\varepsilon_3^p - \varepsilon_2^p)^2}{6}} \\ \varepsilon_3^p \end{Bmatrix} \tag{2}$$

where ε_i^p (i = 1, 2, 3) is the principal plastic strain, [–].

2.1.2. The Models for Rock Elements with Fracture

Once the pre-designed ε_s or ε_t is reached, the rock element falls and a fracture is formed in this element. For a rock element with fracture, it is assumed that it has no plastic strain and only elastic strain is generated. The total elastic strain increment $d\varepsilon_{ij}^t$, which contains the elastic strain increment of the rock matrix $d\varepsilon_{ij}^r$ and fracture $d\varepsilon_{ij}^f$ [42], is expressed as follows:

$$d\varepsilon_{ij}^t = d\varepsilon_{ij}^r + d\varepsilon_{ij}^f \tag{3}$$

It is worth noting that the fracture actually has two cases (a contact and non-contact state), as shown in Figure 1. For the contact state [43], the normal $d\varepsilon_{nc}^f$ and shear $d\varepsilon_{sc}^f$ strains are calculated as follows:

$$\begin{Bmatrix} d\varepsilon_{nc}^f \\ d\varepsilon_{sc}^f \end{Bmatrix} = \begin{bmatrix} 1/(k_n l_c) & 0 \\ 0 & 1/(k_s l_c) \end{bmatrix} \begin{Bmatrix} d\sigma_n \\ d\tau_s \end{Bmatrix} \tag{4}$$

where σ_n and τ_s are, respectively, the normal and shear stresses on the fracture, [Pa]; k_n and k_s are, respectively, the normal and shear stiffness, [Pa/m], and l_c is the characteristic length, [m]. For the non-contact state, both normal and shear stresses are zero. The normal $d\varepsilon_{no}^f$ and shear $d\varepsilon_{so}^f$ strains are calculated as follows:

$$\begin{Bmatrix} d\varepsilon_{no}^f \\ d\varepsilon_{so}^f \end{Bmatrix} = \begin{Bmatrix} -\sigma_n/(K + 4G/3) \\ -\tau_S/2G \end{Bmatrix} \tag{5}$$

where K and G are, respectively, the bulk and shear modulus, [Pa]. The models in this section, which have been verified to be effective for 3D longwall mining in [34], are used to calculate the mining-induced stresses for hydraulic fracturing.

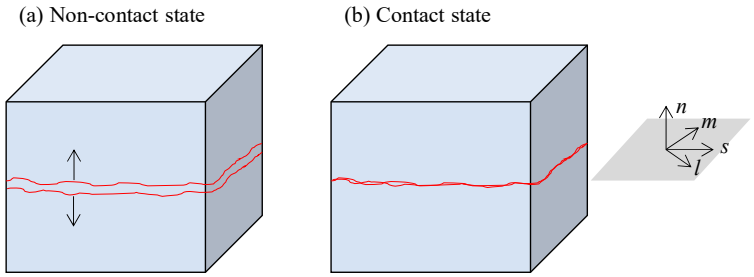


Figure 1. Contact condition of fracture (m, l axis in local coordinate system is decomposed from τ_s): (**a**) non-contact; (**b**) contact. The wavy lines represent the fractures and the arrows imply that the two fracture walls separate.

2.2. Governing Equations Used for Hydraulic Fracturing

Hydraulic fracturing is a complicated hydro-mechanical coupling process, which mainly includes rock deformation, the fluid flow in the fracture, fracture propagation and deflection, flow exchange between rock matrix and fracture. Therefore, the hydro-mechanical coupling must be taken into account, which is not the same as that in Section 2.1. Details are given as follows.

2.2.1. Geo-Mechanical Model

In this section, we also assume that the total rock deformation is the sum of both the deformation of the rock matrix and fracture (Equation (3)). For the deformation of the rock matrix, it is controlled by the following [44]:

$$d\sigma_{ij} + \alpha_b dP_p \delta_{ij} = 2G de_{ij} + \left(K - \frac{2}{3}G\right) d\varepsilon_v \delta_{ij} \tag{6}$$

where α_b is the Biot coefficient, [–]; P_f is the fluid pressure, [Pa]; δ_{ij} is the Kronecker delta; e_{ij} is the strain deviator tensor and ε_v is the bulk strain, [–]. As for the deformation of the fracture, it is also divided into contact and non-contact states, respectively. If the fracture contacts, plastic strain is considered and the strain in Equation (3) can be approximately calculated according to the equivalent continuum theory, as follows [44]:

$$\begin{Bmatrix} d\varepsilon_{nc}^{f'} \\ d\varepsilon_{sc}^{f'} \end{Bmatrix} = \begin{bmatrix} 1/(k_n l_c) & 0 \\ 0 & 1/(k_s l_c) \end{bmatrix} \begin{Bmatrix} d\sigma_n \\ d\tau_s \end{Bmatrix} + \langle F \rangle \begin{Bmatrix} F/k_s l_c \cdot tan\phi \\ \tau_s F/k_s l_c \end{Bmatrix} \tag{7}$$

$$F = \tau_s - [C - \left(\sigma_n + P_f\right) tan\phi] \tag{8}$$

where P_f is the fluid pressure in the fracture, [Pa]; C is the cohesion, [Pa]; ϕ is the dilation angle, [°], and $\langle F \rangle = \begin{cases} 0 \; F < 0 \\ 1 \; F \geq 0 \end{cases}$. If the fracture is in the non-contact state, the fluid pressure equals the normal stress and the shear stress must be zero. Hence, the strain yields according to Hook's law are as follows:

$$\begin{Bmatrix} d\varepsilon_{no}^{f} \\ d\varepsilon_{so}^{f} \end{Bmatrix} = \begin{bmatrix} -\frac{1}{E} & -\frac{v}{E} & -\frac{v}{E} & 0 \\ 0 & 0 & 0 & -\frac{1}{2G} \end{bmatrix} \left\{ dP_f \; d\sigma_{fm} \; d\sigma_{fl} \; d\sigma_{fs} \right\} \tag{9}$$

where n, m and l are the local coordinates. More details of the models are described in [40]. To solve the variables related to stress fields, equilibrium equation Equation (10) and geometric equation Equation (11) are additionally needed.

$$\sigma_{ij,j} + \rho \left(b_i - \frac{dv_i}{dt} \right) = 0 \tag{10}$$

$$\varepsilon_{ij} = \frac{1}{2} \left(u_{i,j} + u_{j,i} \right) \tag{11}$$

where ρ is rock density, [kg/m^3]; b is body force vector per unit volume, [m/s^2], and v is velocity vector, [m/s].

2.2.2. Fracture Flow Model

Laminar flow is assumed for the fracture and the modified cubic flow equation is adopted to express the fluid flow in the fracture [45]:

$$q = -\frac{bw^3}{12\mu} \frac{dP_f}{dL} \tag{12}$$

where q is the flow rate, [m^3/s]; b is the fracture width, [m]; μ is the fluid dynamic viscosity, [Pa · s], and L is the fracture length, [m]. Moreover, the mass conservation equation is also required for solving the pressure distribution. Given that pressure change is significantly affected by the variation in fracture volume, it is assumed that the fluid is incompressible. The mass conservation equation reads as follows:

$$\frac{\partial V_f}{\partial t} + Q_s + \nabla q = 0 \tag{13}$$

where V_f is the fracture volume, [m^3], and Q_s is the source term, [m^3/s].

2.2.3. Fracture Propagation and Orientation

An innovative method was proposed by Ren et al. [40] to make the created fracture surface induced by hydraulic fracturing be visualized, which is adopted for this study. The fracture propagation is controlled by the tensile stress criterion that fracture starts to

propagate when tensile stress exceeds rock tensile strength [46]. For hydraulic fracturing, it is modified with the consideration of fluid pressure, as follows:

$$f = \sigma_3 - P_f - \sigma_t \tag{14}$$

2.2.4. Solution Strategy

Hydraulic fracturing is a complex multi-field coupling problem, and it also requires time to be discrete. Therefore, the solution efficiency and accuracy are impacted by different solving methods such as fully coupling, stepwise coupling and sub-iteration coupling. The full coupling has high consistency and accuracy, but it is time-consuming and is not easy to converge. The stepwise coupling solution has high computational efficiency, but it is only suitable for weak coupling problems. For strong coupling problems such as hydraulic fracturing, large non-convergent iteration errors exist and affect the accuracy of the calculated results. To solve the disadvantages of stepwise coupling, sub-iteration coupling is developed and more sub-iterations are designed in each step for higher computational accuracy. Therefore, the sub-iteration coupling model is adopted in this paper. For the details of this method, see [47,48].

3. Numerical Study on the Hydraulic Fracturing Pattern in Hard Roof

3.1. Modeling Setup

In order to better guide the engineering practice, this study takes the 8101 working face of Datong Mine as the prototype. According to the geological condition in situ, the 3D modeling setup is established after the simplification of rock strata, as shown in Figure 2. The model is in a dimension of 300 m (length) × 250 m (width) × 166 m (height). There are a total of 25 layers in the model, and an ultra-thin layer (0.1 m) is inserted between every two adjacent layers. The vertical distribution in rock strata is listed in Table 1. The coal seam is 7 m away from the bottom of the model. The size of the designed mining area is 180 m × 120 m × 22 m (x, y, z), which is located in the middle of the coal seam and is shown in Figure 2.

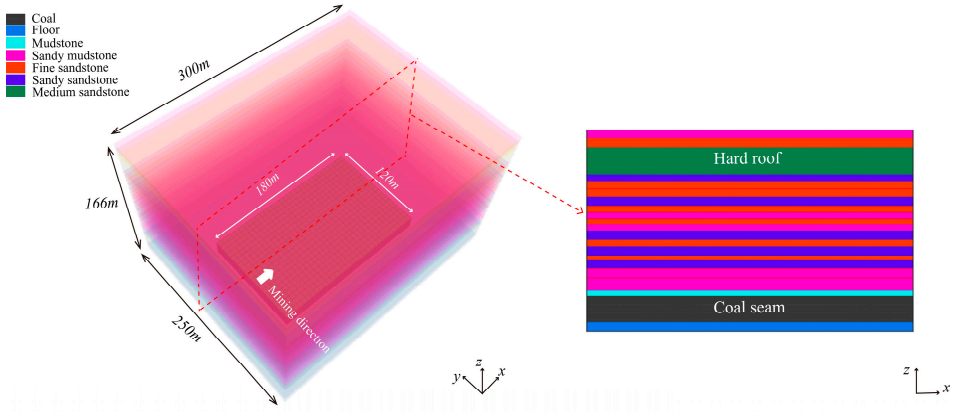


Figure 2. Modeling setup of 3D longwall mining and hydraulic fracturing.

Table 1. Physical and mechanical parameters of 8101 working face after rock strata merger.

No.	Rock Strata	Depth (m)	Thickness (m)	Density (kg/m^3)	Young's Modulus (MPa)	Poisson's Ratio	Cohesion (MPa)	Internal Friction Angle (°)	Tension (MPa)
25	Sandy sandstone	−316	8	2535	23.4	0.22	5.5	33	5.2
24	Medium sandstone	−324	4	2526	14.27	0.17	6.80	31.00	7.00
23	Sandy mudstone	−328	6	2571	8.87	0.2	5.96	32.29	5.84
22	Sandy sandstone	−334	7	2535	23.4	0.22	5.5	33	5.2
21	Medium sandstone	−341	15	2526	14.2	0.17	6.8	31	7
20	Sandy sandstone	−356	6	2535	23.4	0.22	5.5	33	5.2
19	Fine sandstone	−361	5	2585	12.17	0.19	6.51	36.37	5.83
18	Sandy sandstone	−366	6	2535	23.4	0.22	5.5	33	5.2
17	Sandy sandstone	−372	6	2535	23.4	0.22	5.5	33	5.2
16	Fine sandstone	−378	7	2585	12.17	0.19	6.51	36.37	5.83
15	Sandy sandstone	−385	5	2535	23.4	0.22	5.5	33	5.2
14	Sandy mudstone	−390	5	2571	8.87	0.2	5.96	32.29	5.84
13	Sandy sandstone	−395	4	2535	23.4	0.22	5.5	33	5.2
12	Sandy mudstone	−399	5	2571	8.87	0.2	5.96	32.29	5.84
11	Fine sandstone	−404	7	2585	12.17	0.19	6.51	36.37	5.83
10	Sandy sandstone	−411	5	2535	23.4	0.22	5.5	33	5.2
9	Fine sandstone	−416	7	2585	12.17	0.19	6.51	36.37	5.83
8	Sandy sandstone	−423	3	2535	23.4	0.22	5.5	33	5.2
7	Fine sandstone	−426	7	2585	12.17	0.19	6.51	36.37	5.83
6	Sandy mudstone	−433	7	2571	8.87	0.2	5.96	32.29	5.84
5	Sandy mudstone	−440	4	2571	8.87	0.2	5.96	32.29	5.84
4	Sandy mudstone	−444	6	2571	8.87	0.2	5.96	32.29	5.84
3	Mudstone	−450	4	2676	9.87	0.23	5.04	35.45	4.51
2	Coal	−454	20	1426	2.89	0.31	9.50	30.00	2.60
1	Floor	−474	7	2590	23.60	0.18	8.50	31.00	5.20
-	Bedding plane	-	0.1	1000	1	0.1	0.1	20	0.1

3.2. Simulations of Longwall Mining

Rock layers satisfy the constitutive relationship of the rock matrix in Section 2.1.1, while the ultra-thin layers (bedding plane) were regarded as the fracture in the contact state and its discontinuous mechanical behaviors are described in Section 2.1.2. The constitutive parameters of each rock layer are given in Table 1. It should be noted that the 21st layer in the model was set as the hard roof. The gravity effect was considered in the model and the gravity acceleration was set to $-9.8\mathrm{m/s^2}$. The constant stress, which equaled the gravity of the rock strata between the top of the model and the ground surface, was applied to the top face of the model. The remaining boundaries of the model were fixed in their normal directions. The initial stress state of the working face was σ_{xx} = 12 MPa, σ_{yy} = 6.4 MPa and σ_{zz} = 11.4 MPa. The in situ stress field can be numerically reproduced based on the initial state. After the stress balance, longwall mining was started. The cut was located at x = 60 m, and the mining area along the dip (y) was 65 m $\leq y \leq$ 185 m. Each step along the strike (x) was 5 m, with a total of 36 steps. At each step, a sufficient calculation step (40,000) was set to relieve the stress around the gob and to allow the overburden rock to fail.

Two sections, namely 1 and 2, were set to detect the mining-induced stresses, as shown in Figure 3. As for deformation and fractures, they were not the interest of our objective in this paper and thus are not given. Section 1 (y = 125 m) was perpendicular to the y-axis and Section 2 was perpendicular to the x-axis and was located through the center of the mined area. In each section, a monitoring line through the center of the hard roof strata was set to quantitatively illustrate the variations in the mining-induced stresses and a series of monitoring points were arranged in advance to be uniformly spaced with an interval distance of 10 m.

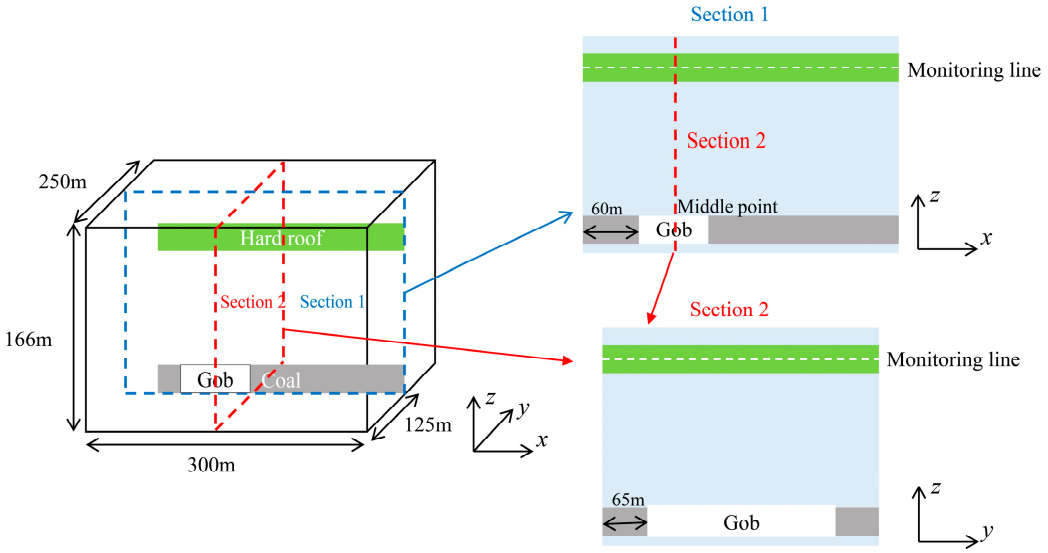


Figure 3. Sketch map of the monitoring plan.

First, it is worth noting that discontinuities are the limitation of this form of modeling; however, 3D longwall mining is still a great challenge for numerical simulations of the mining-induced effects. Figure 4 shows the evolution of vertical stress on monitoring sections at different advancing distances (20 m, 60 m, 100 m, 140m and 200 m). Due to the mining, the stresses around the gob are redistributed in the form of stress release and concentration, which are similar for each advancing distance. However, the disturbed zones where stress release and concentration occur expand with the working face advancing. It is clear that the stress concentration becomes severe during this process, showing that its magnitude progressively increases. For the advancing distance of 20 m, the maximum compressive stress is about 16 MPa, whereas it is 34 MPa for the case of 180 m. In addition, the full stress release zone exhibits an elliptical shape, which seems to be symmetrically distributed along the center of the goaf in each section. These characteristics indicate that the perturbance caused by the mining becomes increasingly stronger in response to continuous advancement, which is the same for mining-induced stresses. For convenience in comparison, the stress variations in the monitoring line for different advancing distances (20 m, 60 m, 100 m, 140 m and 200 m) are quantitatively drawn in Figure 5. The value in the y-axis represents the ratio of abutment stress after mining to that before mining. The abutment stresses along the monitoring line in Section 1 show four-stage shapes characterized by ascending–descending–recovery–stabilization. The stress variations in Section 2 are similar, but it seems that they are symmetrical.

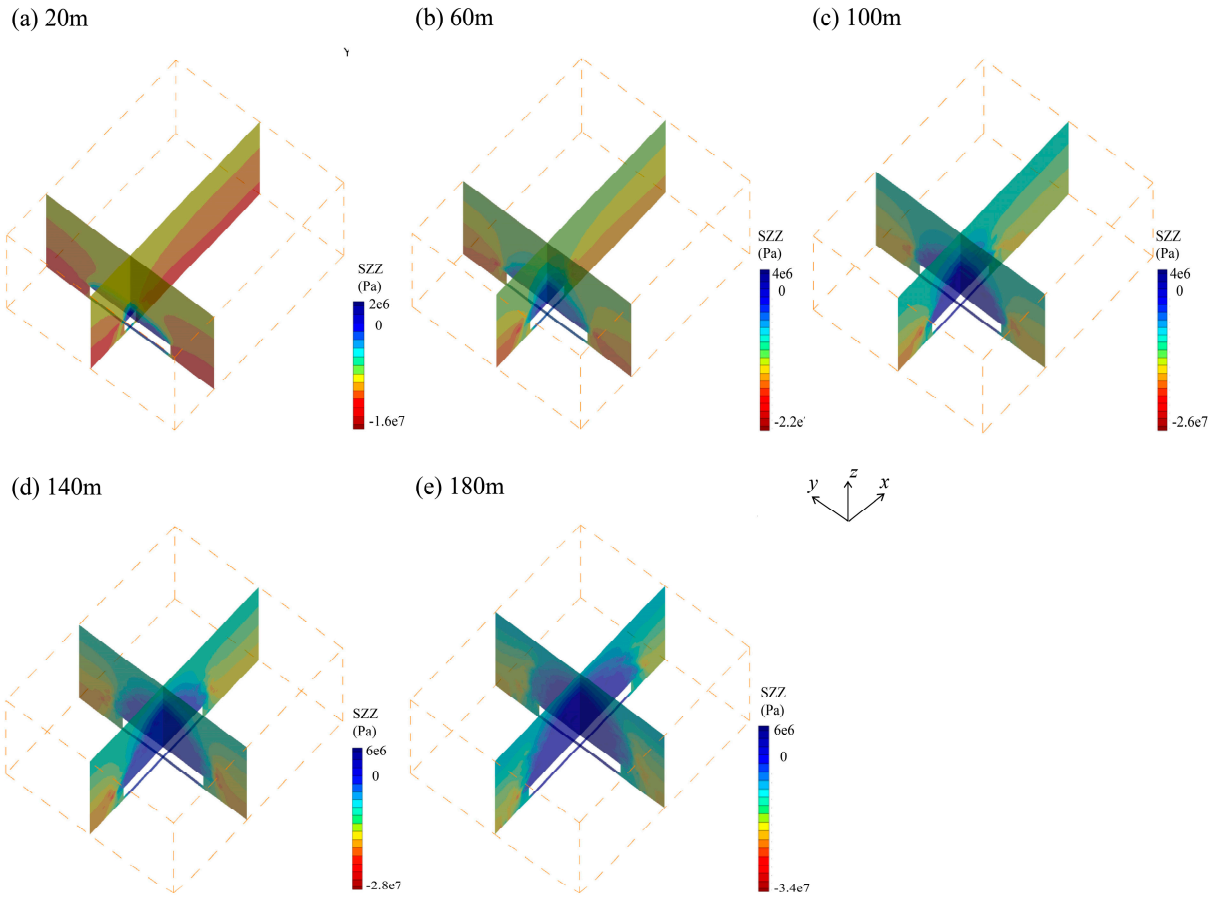


Figure 4. The evolution of vertical stress on monitoring sections in different mining stages.

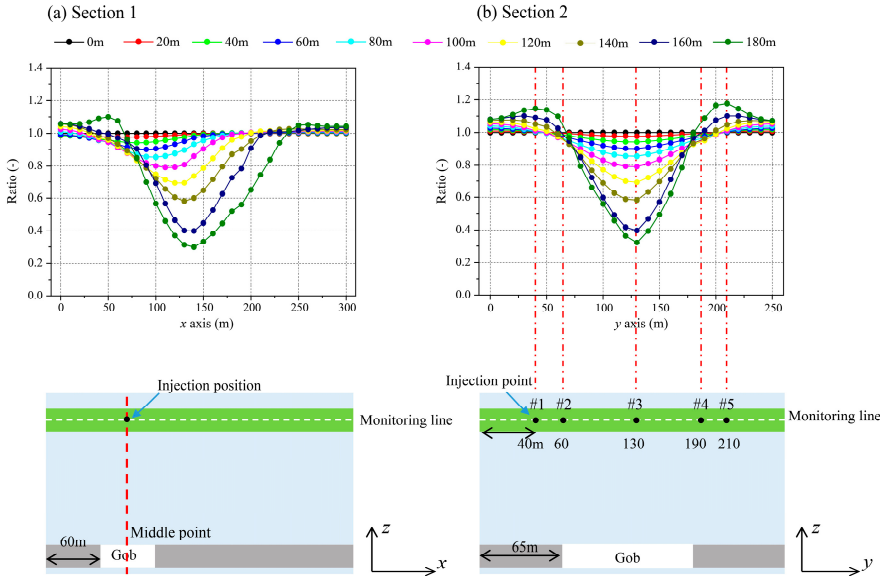


Figure 5. Sketch map of injection positions for hydraulic fracturing above the gob.

3.3. Simulations of Hydraulic Fracturing in the Hard Roof above the Gob

In this section, the fracturing operations were performed above the middle of the gob along the *y*-axis direction. Based on the variations in mining-induced stresses shown in Figure 5, five injection points were designed to explore the influence of mining-induced stresses on hydraulic fracturing patterns. The numbers #1 and #5 were placed in the stress-amending areas ahead of the working face, #2 and #4 were located around the working face

and #3 was situated in the middle. A total volume of 150 m^3 water with an approximate injection rate of 1 m^3/min water was injected into the hard roof. The relevant parameters used are shown in Table 2.

Table 2. Fracture and fluid parameters used in the numerical investigation.

Category	Parameter	Value	Unit
Fracture	Normal stiffness	10	GPa
	Shear stiffness	10	GPa
	Friction angle	30	°
	Cohesion	6	MPa
	Initial aperture	0.01	mm
	Dilation angle	10	°
	Effective conductivity coefficient	0.1	-
Fluid	Dynamic viscosity	0.001	Pa·s
	Density	1000	kg/m^3
	Effective stress coefficient	1	-

Hydraulic fracturing operations were carried out at each advancing distance (20 m, 60 m, 100 m, 140 m and 200 m) and the numerical results are shown in Figure 6. It can be found that the fracturing patterns are not the same in response to the various mining-induced stresses. The fracture propagations on both sides (#1 and #5, #2 and #4) are symmetrical because of the approximately symmetrical mining-induced stresses. Due to the influence of the mining-induced stresses, fracture propagations are strongly perturbed, which becomes more significant for a larger advancing distance. The results demonstrate that the created fractures gradually deflect and become arc-shaped as the advancing distance increases. This is particularly clear for the fracture in the stress-descending area/near the #3 injection point, which deflects the most and gradually propagates along the direction that varies from the vertical to the horizontal. However, the deflection angles of fractures in stress-ascending areas on both sides are relatively small, but they cannot be neglected, especially for a larger advancing distance. In engineering practice, the deflection of the hydraulic fracture could not only horizontally reduce the thickness of the hard roof, but could also vertically cut off the hard roof. This further effectively weakens the integrity of the hard roof and makes it easy to collapse due to stress release.

It is well known that the hydraulic fracture propagates along the direction perpendicular to the minimum principal stress. Therefore, the deflection of the hydraulic fracture is closely related to the variation in the orientation of the minimum principal stress. Figures 7 and 8 depicts the stress magnitudes of each injection point at different advancing distances (20 m, 60 m, 100 m, 140 m and 200 m). In contrast, the perturbance caused by the continuous mining around the #3 injection point is the largest, showing that its magnitudes of the three principal stresses fluctuate the most. In particular, when the advancing distance exceeds 120 m, the minimum principal stress changes from σ_{yy} to σ_{zz}, which indicates that the orientation of the minimum principal stress is transformed from the y-axis direction to the z-axis direction. This phenomenon is in good agreement with the observations in Figure 6. Regarding the points of #1, #2, #4 and #5, the minimum principal stress is always σ_{yy}, which is the main reason for their fractures deflecting less in Figure 6.

Taking the #3 points as a specific example, the directions of the minimum principal stress at different advancing distances (20 m, 60 m, 100 m, 140 m and 200 m) in Sections 1 and 2 in the hard roof are illustrated in Figures 8 and 9, respectively. Note that the shown part in Section 1 is only for the hard roof above the gob whereas the directions for the whole hard roof are given in Section 2. It is directly observed that the orientation of the minimum principal stress is strongly affected by mining-induced stress and the directions at the #3 points progressively deflect to the z-axis direction in either Section 1 or Section 2, which is consistent with the above analysis.

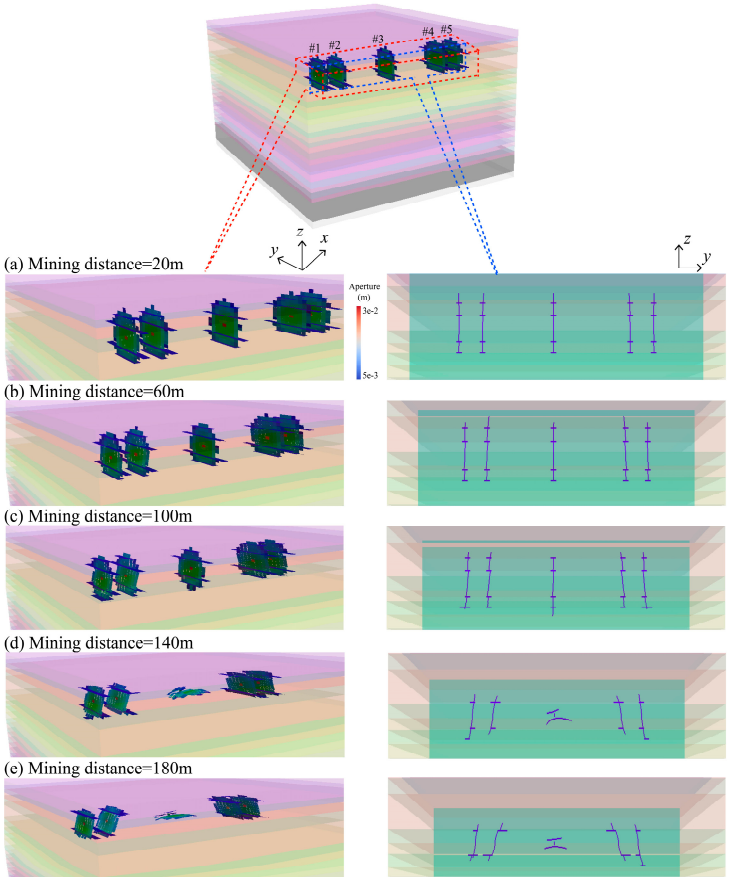


Figure 6. Numerical results of the hydraulic fractures above the gob at different mining distances.

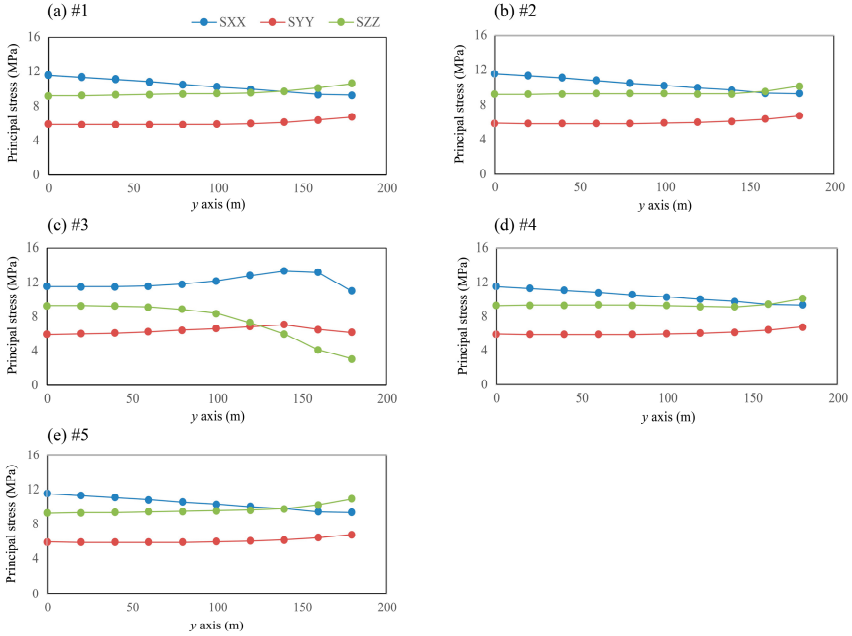


Figure 7. The stress magnitudes of each injection point at different advancing distances.

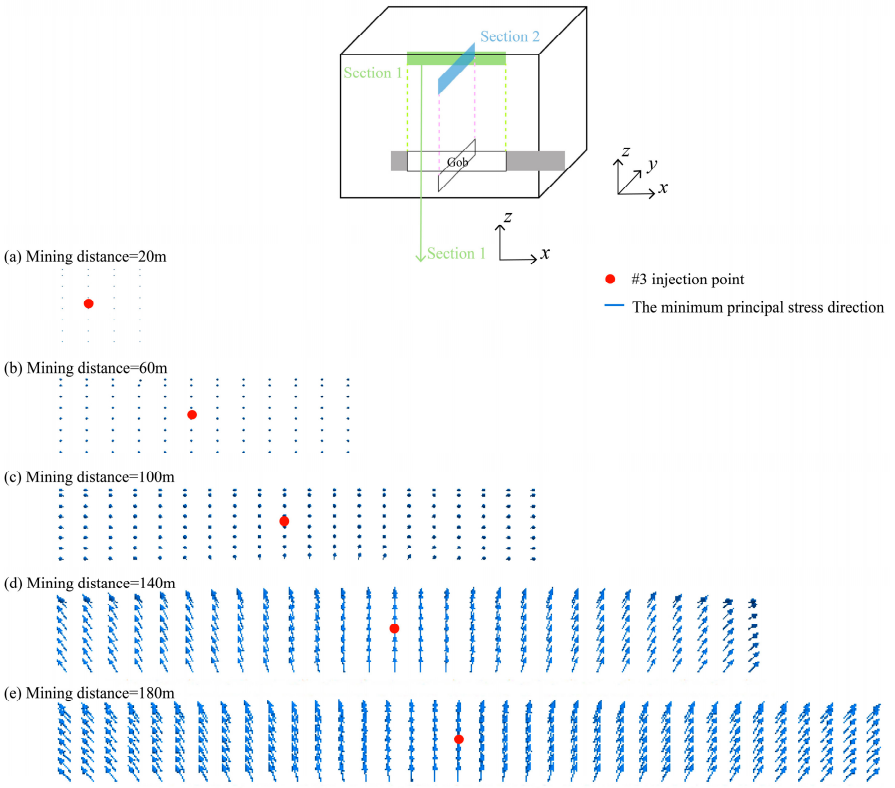


Figure 8. The directions of minor principal stress at different mining distances in Section 1 in the hard roof.

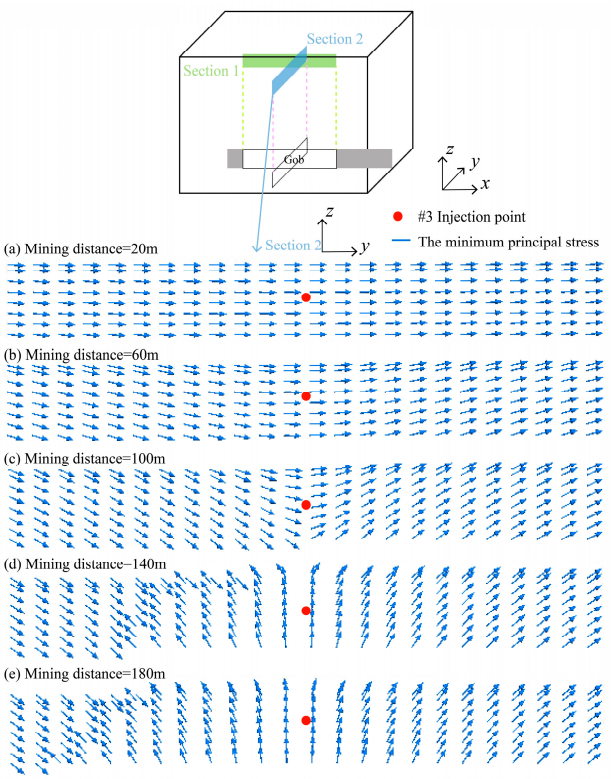


Figure 9. The directions of minor principal stress at different mining distances in Section 2 in the hard roof.

3.4. Simulations of Hydraulic Fracturing in Hard Roof ahead of the Working Face

Based on the results in Section 3.3, it is clear that when the advancing distance exceeds 120 m, the mining-induced stresses become significant and can largely affect the hydraulic fracturing pattern. Thus, in this section the advancing distance is arbitrarily fixed to 140 m, and we are focused on the influence of the mining-induced stresses ahead of the working face on the hydraulic fracturing pattern. Three injection points are situated in Section 2, being 20 m, 40 m and 60 m away from the working face, as shown in Figure 10. The calculated results of the hydraulic fracturing patterns at different injection points for the advancing distance of 140 m are given in Figure 11. It is found that the hydraulic fracturing pattern at each injection point is similar and the deflection along the propagation direction is rather small. The directions of the minimum principal stress at each injection point are shown in Figure 12. Figure 12 depicts that the directions of the minimum principal stress do not practically change, indicating that the defection of the hydraulic fracturing pattern caused by mining-induced stress is not significant in the hard roof.

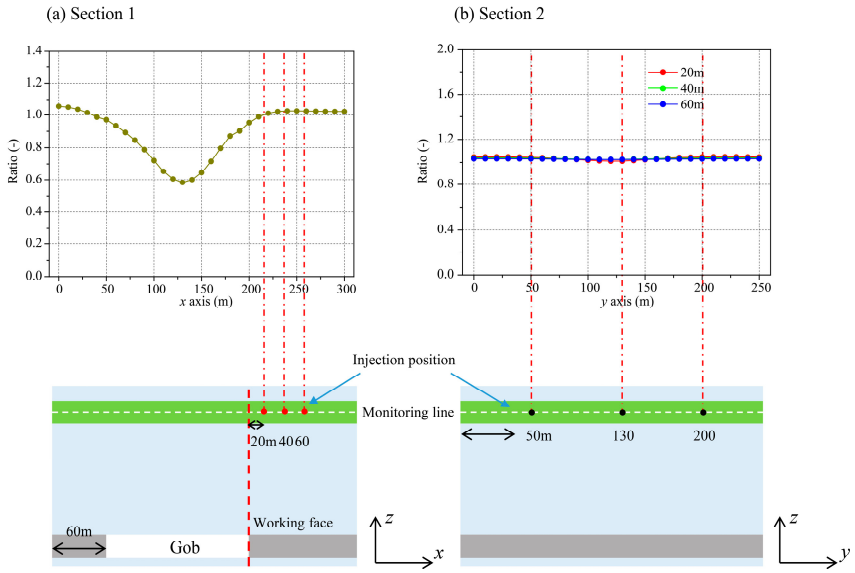


Figure 10. Sketch map of injection positions for hydraulic fracturing ahead of the working face.

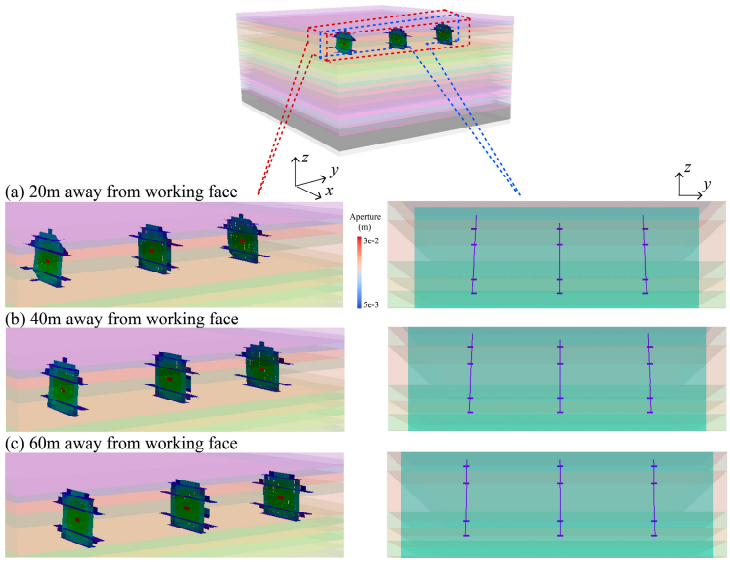


Figure 11. Numerical results of hydraulic fracturing patterns at different injection points ahead of the working face for the advancing distance of 140 m.

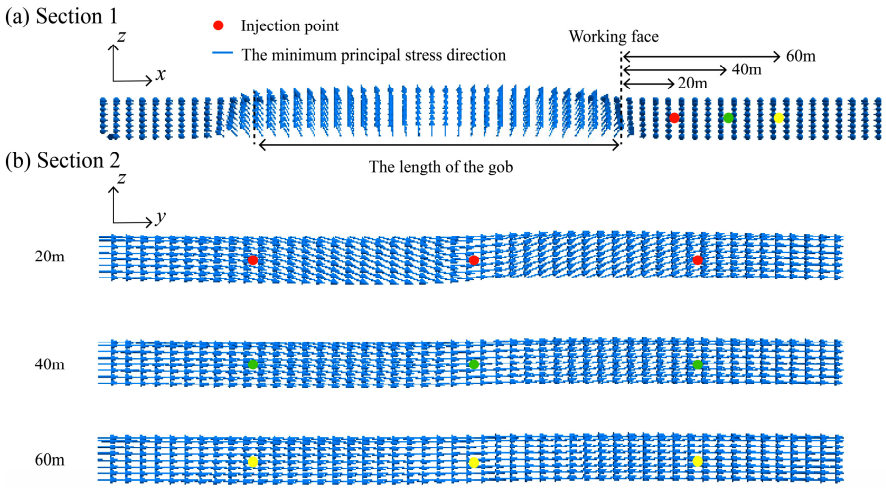


Figure 12. The directions of minimum principal stress in the hard roof at different injection points ahead of the working face for the advancing distance of 140 m.

3.5. Sensitivity Analysis

The sensitivity of the geological conditions on the propagation of hydraulic fractures is important for the optimization of the hydraulic fracturing operations in engineering design. In this section, we primarily focus on the parameters that often appear in situ and that have not been taken into account on the 3D scale, including the position of the hard roof, the stress difference and the initial minimum principal stress direction. The hydraulic fracturing operation in Section 3.4 is adopted as the base case for the sensitivity analysis in this section.

3.5.1. Effect of the Position of the Hard Roof

In Section 3.4, it was shown that the hydraulic fracturing pattern is not strongly impacted by mining-induced stress, where the hard roof is far away from the coal seam. In general, the mining-induced effect constantly degrades with the increase in the distance away from the roof. Therefore, in order to explore the characteristics of the hydraulic fracture in the low hard roof (which is closer to the coal seam) in response to the mining-induced stress, the fifth, sixth and seventh strata in Figure 2 were artificially set as hard roof, and the original hard roof strata (the 21st layer) was set as non-key strata. The relevant parameters and methods of numerical calculation were the same as that in Section 3.4.

Figure 13 shows the evolution of the vertical stress ratio on monitoring sections at different advancing distances (20 m, 60 m, 100 m, 140 m and 200 m). Compared to the characteristics in Figure 5, the mining-induced stresses are more significant in the low hard roof, showing that the magnitude of the vertical stress ratio at the same position is larger and fluctuates more. In particular, the stress-disturbed range (stress-ascending area, stress-descending area and rock stability area) ahead of the working face increases. For convenience in comparison, hydraulic fracturing operations were also set to the same as those in Section 3.4.

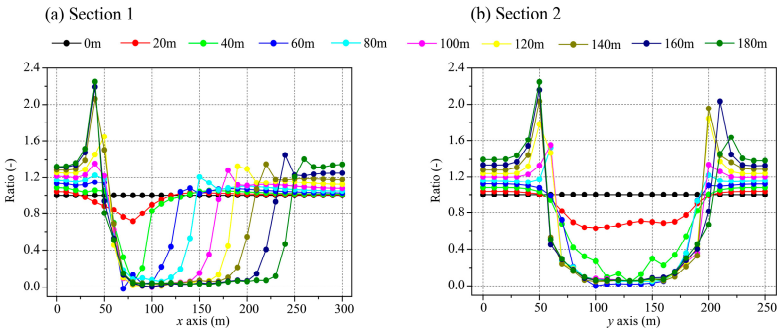


Figure 13. The evolution of vertical stress on monitoring lines in different mining stages.

The calculated results of the hydraulic fracturing patterns at different injection points in the low hard roof for the advancing distance of 140 m are illustrated in Figure 14. It can be seen that the influence of the mining-induced stress on the hydraulic fracture propagation at the middle of the injection points is the largest, where the hydraulic fracture is generated in the arc-shaped form. However, vertical fractures on both sides are formed. This implies that if in situ the fracturing points are set ahead of the middle working face, the mining-induced stress should be fully considered. In addition, when the distance between the injection point and the working face exceeds 40 m, the hydraulic fracturing pattern does not practically vary any more.

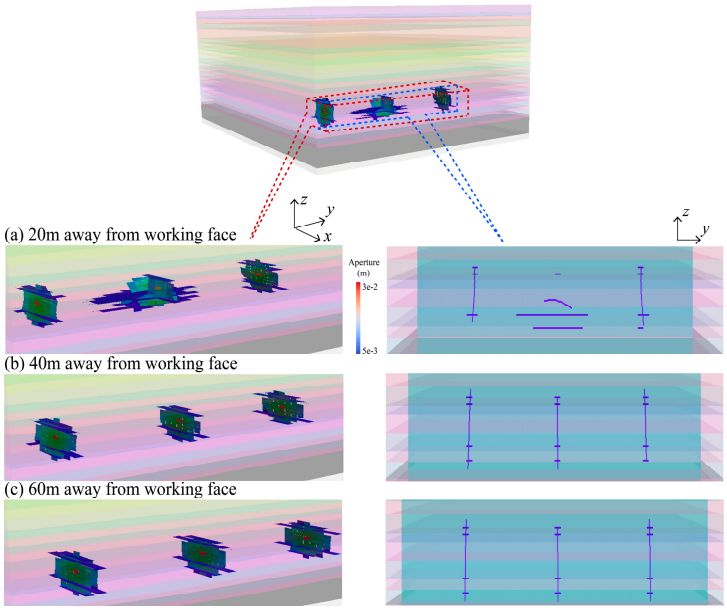


Figure 14. Numerical results of hydraulic fracturing patterns at different injection points ahead of the working face for the advancing distance of 140 m in the low hard roof.

The directions of the minimum principal stresses corresponding to Figure 14 are given in Figure 15. As shown in Figure 15, the directions are significantly disturbed ahead of the working face, especially in the middle. However, this disturbance decreases as the distance between the injection point and the working face increases. These characteristics are consistent with the observations in Figure 14. By comparing Figures 11 and 14, for the hard roof closer to the coal seam, the fracturing propagation deflects more and the created fracturing pattern is more complex, which implies that the hydraulic fracturing operation in situ is disturbed more.

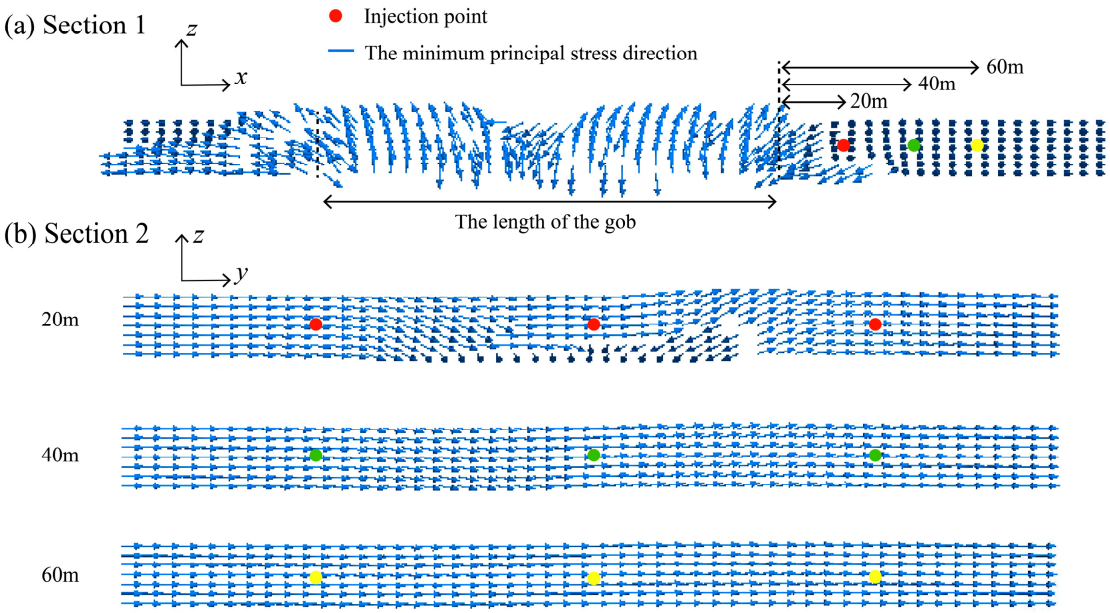


Figure 15. The directions of minimum principal stress in the hard roof at different injection points ahead of the working face for the advancing distance of 140 m in the low hard roof.

3.5.2. Effect of the Stress Difference between the Maximum and Minimum Principal Stresses

The ground stress has a great influence on the distribution characteristics of mining-induced stress, which in turn affects the hydraulic fracture propagation in the hard roof. In this section, the initial σ_{zz} and σ_{xx} imposed to the coal seam were fixed (σ_{xx} = 12 MPa and σ_{zz} = 11.4 MPa), but σ_{yy} was progressively increased from 6.4 MPa to 10 MPa. In each case, the ground stress field was inverted based on the imposed stress of the coal seam. After stress balance was reached, the longwall mining was simulated and then the fracturing operation was performed the same as that in Section 3.4. In this section, the advancing distance was set to be 140m and only the fracturing pattern at the fracturing position of 20 m ahead of the working face is given. Figure 16 shows the calculated results for different stress differences. It is observed that as σ_{yy} increases from 6.4 MPa to 10 MPa, the deflection angle at each injection point increases, especially for that in the middle, which is deflected from the vertical fracture to the horizontal arc-shaped fracture. The cutting degree of the hard roof increases and the stratification effect is enhanced. The directions of the minimum principal stress corresponding to Figure 16 are demonstrated in Figure 17. It is clear that when σ_{yy} is increased to 10 MPa, the directions of the minimum principal stress are perturbed more by mining-induced stress and the deflection increases sharply, showing that those near the middle point in Section 2 change from the y-axis direction to the z-axis direction. In addition, the disturbed range expands wider for σ_{yy} = 10 MPa. For example, the directions in Section 1 near 20 m, indicated in Figure 17a, do not deflect, whereas a larger deflection is observed in Figure 17b.

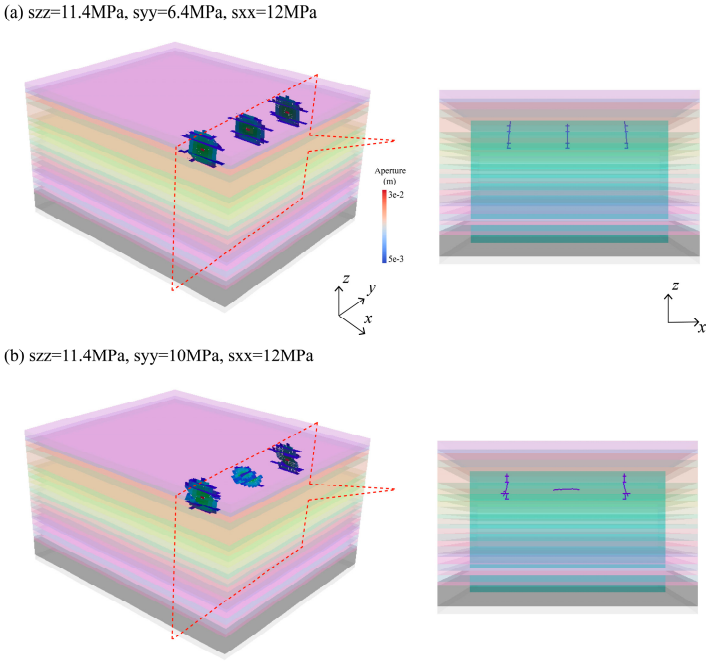


Figure 16. Numerical results of hydraulic fracturing patterns at different injection points ahead of the working face for the advancing distance of 140 m for different stress differences.

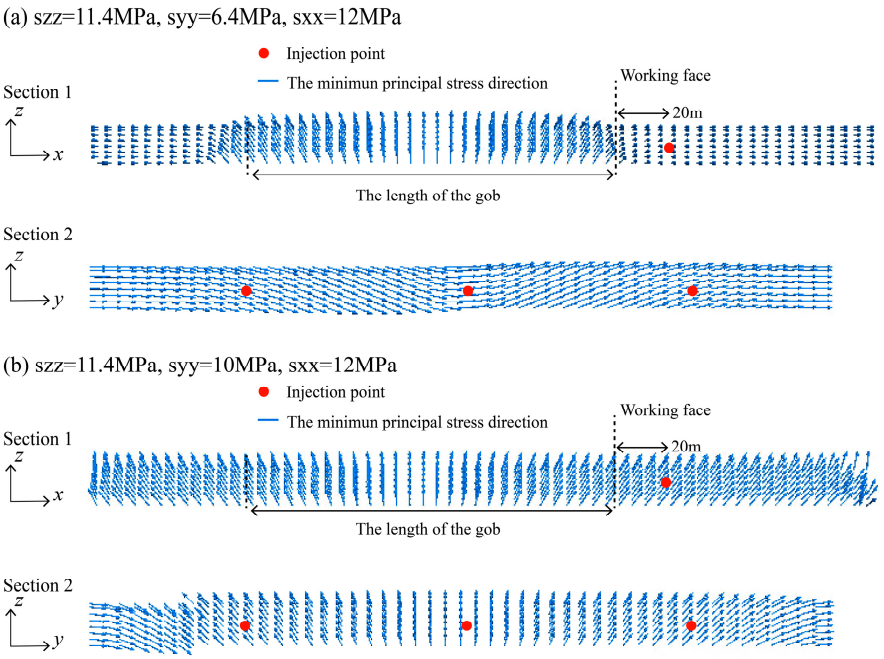


Figure 17. The directions of minimum principal stress in the hard roof at different injection points ahead of the working face for the advancing distance of 140 m for different stress differences.

3.5.3. Effect of the Initial Minimum Principal Stress Direction

The initial stress state of the working face was σ_{xx} = 12 MPa, σ_{yy} = 6.4 MPa and σ_{zz} = 11.4 MPa. In this section, the stress states of σ_{xx} = 12 MPa, σ_{yy} = 6.4 MPa and σ_{zz} = 11.4 MPa were adopted for comparison to examine the effect of the initial minimum principal stress direction on the hydraulic fractures. The other conditions were the same as that in Section 3.4. Figure 18 compares the calculated results of different minimum principal stress directions. It is found that when the minimum principal stress is converted to σ_{zz},

the fracture propagation is clearly changed, which is deflected from the vertical fracture to the oblique arc fracture.

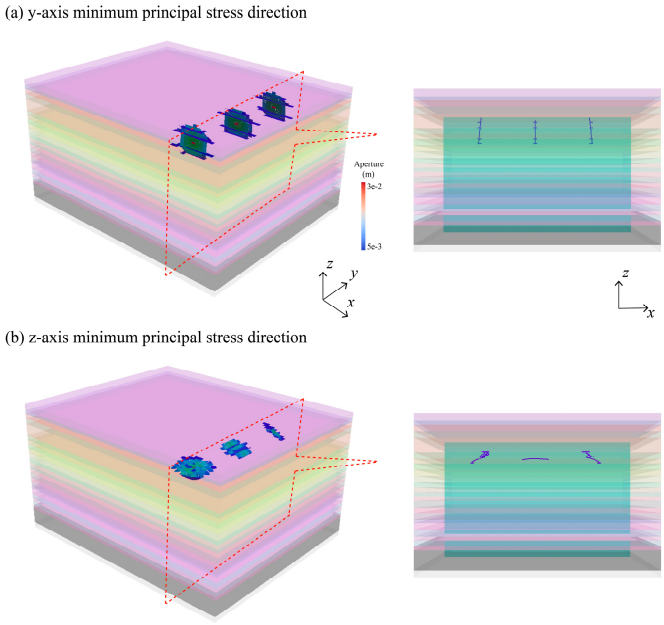


Figure 18. Numerical results of hydraulic fracturing patterns at different injection points ahead of the working face for the advancing distance of 140 m for different initial directions of the minimum principal stress.

The directions of the minimum principal stress corresponding to Figure 18 are demonstrated in Figure 19. It is clear that when the minimum principal stress is converted to σ_{zz}, the disturbed range is extended, which is shown as follows: the directions in Section 1 near 20 m, indicated in Figure 19a, do not deflect, whereas a larger deflection is observed in Figure 19b. It seems that the initial minimum principal stress direction affects the created fractures more and the details are discussed in the next section.

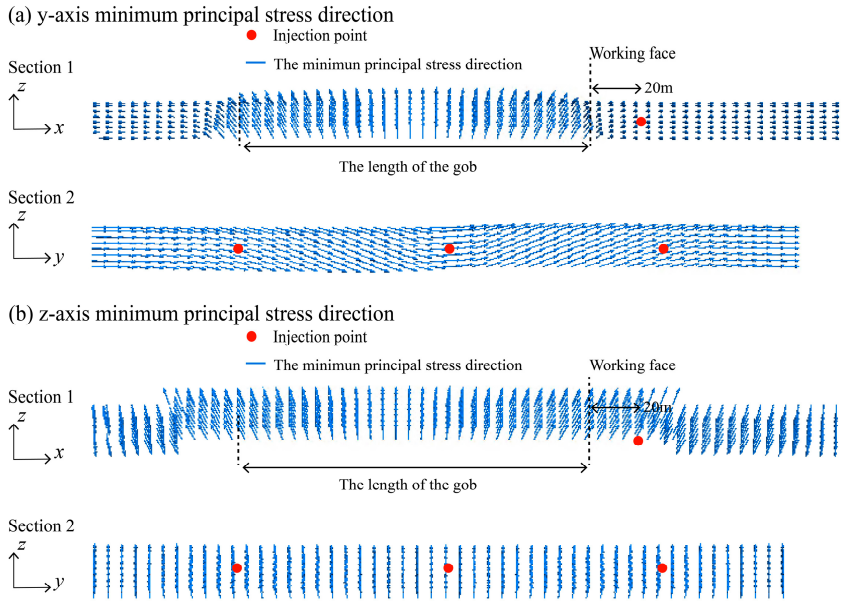


Figure 19. The directions of minimum principal stress in the hard roof at different injection points ahead of the working face for the advancing distance of 140 m for different initial directions of the minimum principal stress.

4. Discussion

In this study, taking the 8101 working face of Tashan Coal Mine with a hard roof problem as the example, the longwall mining was simulated and hydraulic fracturing operations were performed in different areas, namely the stress-ascending area, stress-descending area and stress-stable area, respectively. Due to the mining-induced effect, the hydraulic fracture was accompanied by a certain degree of deflection forming arc-shaped fractures, and the deflection angle progressively increased with the continuous working face advancing. Taking the advancing distance of 140 m as an example, the deflection angle at each injection point above the gob is shown in Figure 20. It is seen that the deflection angle in the stress-descending area is the largest, which reaches over 80°. However, it is approximately 35° for the stress-ascending area and about 25° for the stress-stable area. Due to the invisible underground situation and the limitation of the monitoring device, this phenomenon of deflection in hydraulic fracture propagation is difficult to be observed in situ. However, it was captured via laboratory physical simulation [37]. It was found in [37] that the hydraulic fracture is gradually deflected when subjected to stress concentration caused by the coal pillar, which is similar with the case of the hard roof and can confirm the correctness of the simulated results in this paper to some extent.

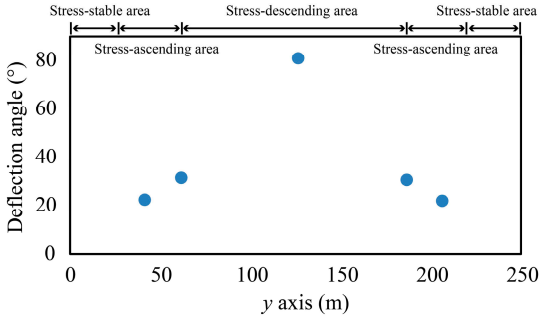


Figure 20. The deflection angle at each injection point above the gob after hydraulic fracturing.

Sensitivity analysis of the geological conditions on the propagation of hydraulic fractures ahead of the working face was studied and the results are summarized in Figure 21. Note that the average value of the deflection angles on both sides is adopted for quantitative comparison. It is shown that the closer to the coal seam and the smaller the difference between the maximum and minimum principal stresses, the greater the deflection angle of the hydraulic fracture. In addition, the initial minimum principal stress direction should be fully considered for hydraulic fracturing optimization. In contrast, the stress difference has the greatest influence on the fracture deflection, followed by the initial minimum principal stress direction, and the hard roof position has the least influence. In practice, the controllable fracture complexity is positively corelated with the weakening effect in the hard roof. However, an actual geological condition such as stress distribution is rather complicated and could strongly affect the fracturing networks, which is often a challenge in the deep. The obtained results could provide meaningful guidance for directional hydraulic fracturing and improve the safety level in mining.

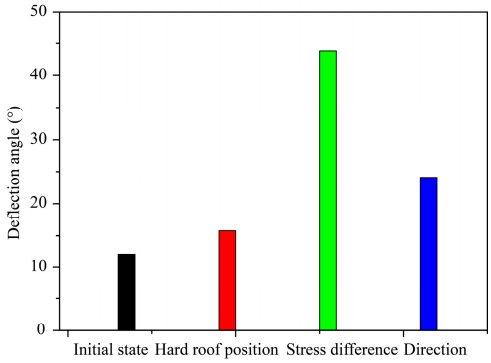


Figure 21. Comparisons of the deflection angle after hydraulic fracturing with different geological factors.

5. Conclusions

In this paper, we used the models recently developed by Chen et al. [39] and Ren et al. [40], which were implemented into the finite-difference 3D dynamic time-marching explicit code, for the numerical simulations. By using the numerical model, the propagation of hydraulic fractures in the hard roof was systematically studied. Based on the calculated results, a better understanding of the spatial fracture propagation behavior was achieved and the main conclusions are as follows:

(1) The stress field around the gob is strongly perturbed due to the mining. After the extraction of the coal seam, the stress field around the mined-out area is redistributed in the form of stress release and concentration showing a four-stage shape characterized by ascending–descending–recovery–stabilization above the coal seam. The principal stress directions are strongly perturbed as well. The mining-induced effect gradually increases with the continuous working face advancing.

(2) Mining-induced stress could significantly affect the propagation of the hydraulic fracture. Due to the mining-induced stress, the hydraulic fracture starts to deflect and gradually becomes arc-shaped as the advancing distance increases. The deflection that occurs in the stress-descending area is clearly larger in comparison with that in both stress-ascending and stress-stable areas. The main reason for these features is that the changes in the principal stress direction vary in different disturbed areas. In addition, no matter whether hydraulic fracturing is designed above the gob or ahead of the working face, operation in the areas close to the middle of the gob is preferable where the created fractures would be more arc-shaped.

(3) Mining-induced stress differs with the variations in geological conditions imposed to the target strata. This further impacts the propagation of the hydraulic fracture and should be fully considered in engineering practice. Sensitivity analysis shows that the difference between the maximum and minimum principal stress gives the fracture a larger deflection compared to the initial minimum principal stress direction and hard roof position. Exact geological data are essential for practical hydraulic fracturing operations.

Author Contributions: Conceptualization, J.C.; methodology, Z.Q.; software, L.Z.; writing—original draft preparation, X.S. All authors have read and agreed to the published version of the manuscript.

Funding: The research was financially supported by the Natural Science Foundation of Sichuan Province (No. 2022NSFSC1169), the Scientific Research Foundation of Xihua University (No. Z211014), the Natural Science Foundation Project of Chongqing (No. cstc2021jcyj-msxmX0929) and the National Natural Science Foundation of China (U21A2030).

Data Availability Statement: The manuscript data used to support the findings of this study are available from the corresponding author upon request.

Conflicts of Interest: The authors declare that they have no conflict of interest.

References

1. Liu, J.; Liu, C.; Yao, Q.; Si, G. The position of hydraulic fracturing to initiate vertical fractures in hard hanging roof for stress relief. *Int. J. Rock Mech. Min. Sci.* **2020**, *132*, 104328. [CrossRef]
2. Song, X.M.; Lian, Q.W.; Xing, P.W.; Fu, Y.P.; Li, Z.J. Research on air bumping disaster induced by large roof falling in goaf. *Coal Sci. Technol.* **2009**, *37*, 1–4. [CrossRef]
3. Qi, Q.X.; Li, X.L.; Zhao, S.K. Theory and practices on stress control of mine pressure bumping. *Int. J. Coal Sci. Technol.* **2013**, *41*, 1–5. [CrossRef]
4. Jiang, Y.D.; Pan, Y.S.; Jiang, F.X.; Dou, L.M.; Ju, Y. LM State of the art review on mechanism and prevention of coal bumps in China. *J. China Coal Soc.* **2014**, *39*, 205–213. [CrossRef]
5. Dou, L.M.; He, J.; Cao, A.Y.; Gong, S.Y.; Cai, W. Rock burst prevention methods based on theory of dynamic and static combined load induced in coal mine. *J. China Coal Soc.* **2015**, *40*, 1469–1476. [CrossRef]
6. Lu, C.-P.; Liu, G.-J.; Liu, Y.; Zhang, N.; Xue, J.-H.; Zhang, L. Microseismic multi-parameter characteristics of rockburst hazard induced by hard roof fall and high stress concentration. *Int. J. Rock Mech. Min. Sci.* **2015**, *76*, 18–32. [CrossRef]
7. Wang, Q.; Wang, H.; Qi, Z. An application of nonlinear fuzzy analytic hierarchy process in safety evaluation of coal mine. *Saf. Sci.* **2016**, *86*, 78–87. [CrossRef]
8. Zhang, J.; Li, B.; Zhou, N.; Zhang, Q. Application of solid backfilling to reduce hard-roof caving and longwall coal face burst potential. *Int. J. Rock Mech. Min. Sci.* **2016**, *88*, 197–205. [CrossRef]
9. Clark, J. A Hydraulic Process for Increasing the Productivity of Wells. *J. Pet. Technol.* **1949**, *1*, 1–8. [CrossRef]
10. Puri, R.; King, G.; Palmer, I. Damage to coal permeability during hydraulic fracturing. In *Low Permeability Reservoirs Symposium*; Society of Petroleum Engineers; OnePetro: Richardson, TX, USA, 1991.
11. Wright, C.; Tanigawa, J.; Shixin, M.; Li, Z. Enhanced hydraulic fracture technology for a coal seam reservoir in Central China. In *International Meeting on Petroleum Engineering*; Society of Petroleum Engineers; OnePetro: Richardson, TX, USA, 1995.
12. Zhai, C.; Li, M.; Sun, C.; Zhang, J.; Yang, W.; Li, Q. Guiding-controlling technology of coal seam hydraulic fracturing fractures extension. *Int. J. Min. Sci. Technol.* **2012**, *22*, 831–836. [CrossRef]
13. Liu, Y.; Lebedev, M.; Zhang, Y.; Wang, E.; Li, W.; Liang, J.; Feng, R.; Ma, R. Micro-Cleat and Permeability Evolution of Anisotropic Coal During Directional CO_2 Flooding: An In Situ Micro-CT Study. *Nat. Resour. Res.* **2022**, *31*, 2805–2818. [CrossRef]
14. Liu, Y.; Wang, E.; Jiang, C.; Zhang, D.; Li, M.; Yu, B.; Zhao, D. True Triaxial Experimental Study of Anisotropic Mechanical Behavior and Permeability Evolution of Initially Fractured Coal. *Nat. Resour. Res.* **2023**, *32*, 1–19. [CrossRef]
15. Chernov, O.I. Hydrodynamic stratification of petrologically uniform strong rocks as a means of controlling intransigent roofs. *J. Min. Sci.* **1982**, *18*, 102–107. [CrossRef]
16. Fan, J.; Dou, L.; He, H.; Du, T.; Zhang, S.; Gui, B.; Sun, X. Directional hydraulic fracturing to control hard-roof rockburst in coal mines. *Int. J. Min. Sci. Technol.* **2012**, *22*, 177–181. [CrossRef]
17. Jeffrey, R.; Chen, Z.; Mills, K.; Pegg, S. Monitoring and measuring hydraulic fracturing growth during preconditioning of a roof rock over a coal longwall panel. In *ISRM International Conference for Effective and Sustainable Hydraulic Fracturing*; International Society for Rock Mechanics; OnePetro: Richardson, TX, USA, 2013.
18. Yu, B.; Zhao, J.; Kuang, T.; Meng, X. In situ investigations into overburden failures of a super-thick coal seam for longwall top coal caving. *Int. J. Rock Mech. Min. Sci.* **2015**, *78*, 155–162. [CrossRef]
19. He, J.; Dou, L.-M.; Mu, Z.-L.; Cao, A.-Y.; Gong, S.-Y. Numerical simulation study on hard-thick roof inducing rock burst in coal mine. *J. Cent. South Univ.* **2016**, *23*, 2314–2320. [CrossRef]
20. Wang, G.-F.; Gong, S.-Y.; Li, Z.-L.; Dou, L.-M.; Cai, W.; Mao, Y. Evolution of Stress Concentration and Energy Release Before Rock Bursts: Two Case Studies from Xingan Coal mine, Hegang, China. *Rock Mech. Rock Eng.* **2016**, *49*, 3393–3401. [CrossRef]
21. Yu, B. Behaviors of overlying strata in extra-thick coal seams using top-coal caving method. *J. Rock Mech. Geotech. Eng.* **2016**, *8*, 238–247. [CrossRef]
22. Yu, B.; Zhao, J.; Xiao, H. Case Study on Overburden Fracturing during Longwall Top Coal Caving Using Microseismic Monitoring. *Rock Mech. Rock Eng.* **2017**, *50*, 507–511. [CrossRef]
23. Lu, Y.; Gong, T.; Xia, B.; Yu, B.; Huang, F. Target Stratum Determination of Surface Hydraulic Fracturing for Far-Field Hard Roof Control in Underground Extra-Thick Coal Extraction: A Case Study. *Rock Mech. Rock Eng.* **2018**, *52*, 2725–2740. [CrossRef]
24. Yu, B.; Gao, R.; Kuang, T.; Huo, B.; Meng, X. Engineering study on fracturing high-level hard rock strata by ground hydraulic action. *Tunn. Undergr. Space Technol.* **2019**, *86*, 156–164. [CrossRef]
25. Shimada, H.; Mastui, K.; Anwar, H. Control of hard-to-collapse massive roofs in longwall faces using a hydraulic fracturing techniques. In Proceedings of the 17th International Conference on Ground Control in Mining, Morgantown, WV, USA, 31 December 1998; pp. 79–87.
26. Hayes, P. Moonee Colliery: Renewing the economic viability of a mine using microseismic and hydraulic fracturing techniques in massive roof conditions. In Proceedings of the 19th International Conference on Ground Control in Mining, Morgantown, WV, USA, 8–10 August 2000; pp. 38–44.
27. Huang, B.; Wang, Y.; Cao, S. Cavability control by hydraulic fracturing for top coal caving in hard thick coal seams. *Int. J. Rock Mech. Min. Sci.* **2015**, *74*, 45–57. [CrossRef]
28. Kang, H.; Lv, H.; Gao, F.; Meng, X.; Feng, Y. Understanding mechanisms of destressing mining-induced stresses using hydraulic fracturing. *Int. J. Coal Geol.* **2018**, *196*, 19–28. [CrossRef]

29. He, Q.; Suorineni, F.T.; Ma, T.; Oh, J. Effect of discontinuity stress shadows on hydraulic fracture re-orientation. *Int. J. Rock Mech. Min. Sci.* **2017**, *91*, 179–194. [CrossRef]
30. Li, Y.; Long, M.; Tang, J.; Chen, M.; Fu, X. A hydraulic fracture height mathematical model considering the influence of plastic region at fracture tip. *Pet. Explor. Dev.* **2020**, *47*, 184–195. [CrossRef]
31. Zhang, J.; Li, Y.; Pan, Y.; Wang, X.; Yan, M.; Shi, X.; Zhou, X.; Li, H. Experiments and analysis on the influence of multiple closed cemented natural fractures on hydraulic fracture propagation in a tight sandstone reservoir. *Eng. Geol.* **2021**, *281*, 105981. [CrossRef]
32. Ju, Y.; Wang, Y.; Su, C.; Zhang, D.; Ren, Z. Numerical analysis of the dynamic evolution of mining-induced stresses and fractures in multilayered rock strata using continuum-based discrete element methods. *Int. J. Rock Mech. Min. Sci.* **2019**, *113*, 191–210. [CrossRef]
33. Zhang, B.; Sun, H.; Liang, Y.; Wang, K.; Zou, Q. Characterization and Quantification of Mining-Induced Fractures in Overlying Strata: Implications for Coalbed Methane Drainage. *Nat. Resour. Res.* **2019**, *29*, 2467–2480. [CrossRef]
34. Chen, J.; Zhou, L.; Xia, B.; Su, X.; Shen, Z. Numerical Investigation of 3D Distribution of Mining-Induced Fractures in Response to Longwall Mining. *Nat. Resour. Res.* **2021**, *30*, 889–916. [CrossRef]
35. Xu, C.; Yuan, L.; Cheng, Y.; Wang, K.; Zhou, A.; Shu, L. Square-form structure failure model of mining-affected hard rock strata: Theoretical derivation, application and verification. *Environ. Earth Sci.* **2016**, *75*, 1180. [CrossRef]
36. Li, N.; Wang, E.Y.; Ge, M.C.; Liu, J. The fracture mechanism and acoustic emission analysis of hard roof: A physical modeling study. *Arab. J. Geosci.* **2015**, *8*, 1895–1902. [CrossRef]
37. Xia, B.; Zhang, X.; Yu, B.; Jia, J. Weakening effects of hydraulic fracture in hard roof under the influence of stress arch. *Int. J. Min. Sci. Technol.* **2018**, *28*, 951–958. [CrossRef]
38. He, Q.; Suorineni, F.T.; Oh, J. Strategies for Creating Prescribed Hydraulic Fractures in Cave Mining. *Rock Mech. Rock Eng.* **2016**, *50*, 967–993. [CrossRef]
39. Chen, J.; Zhou, L.; Chemenda, A.I.; Xia, B.; Su, X.; Shen, Z. Numerical modeling of fracture process using a new fracture constitutive model with applications to 2D and 3D engineering cases. *Energy Sci. Eng.* **2020**, *8*, 2628–2647. [CrossRef]
40. Ren, X.; Zhou, L.; Li, H.; Lu, Y. A three-dimensional numerical investigation of the propagation path of a two-cluster fracture system in horizontal wells. *J. Pet. Sci. Eng.* **2019**, *173*, 1222–1235. [CrossRef]
41. Itasca Consulting Group. *FLAC 3D (Fast Lagrangian Analysis of Continua in 3-Dimensions)*; 5.0 Manual; Itasca Consulting Group: Minneapolis, MN, USA, 2013.
42. Oliver, J. Modelling strong discontinuities in solid mechanics via strain softening constitutive equations. Part 2: Numerical simulation. *Int. J. Numer. Methods Eng.* **2015**, *39*, 3601–3623. [CrossRef]
43. Goodman, R.E.; Taylor, R.L.; Brekke, T.L. A Model for the Mechanics of Jointed Rock. *J. Soil Mech. Found. Div.* **1968**, *94*, 637–659. [CrossRef]
44. Zhou, L.; Su, X.; Lu, Y.; Ge, Z.; Zhang, Z.; Shen, Z. A New Three-Dimensional Numerical Model Based on the Equivalent Continuum Method to Simulate Hydraulic Fracture Propagation in an Underground Coal Mine. *Rock Mech. Rock Eng.* **2018**, *52*, 2871–2887. [CrossRef]
45. Zimmerman, R.W.; Kumar, S.; Bodvarsson, G.S. Lubrication theory analysis of the permeability of rough-walled fractures. *Int. J. Rock Mech. Min. Sci. Geomech. Abstr.* **1991**, *28*, 325–331. [CrossRef]
46. Barenblatt, G.I. The Mathematical Theory of Equilibrium Cracks in Brittle Fracture. *Adv. Appl. Mech.* **1962**, *7*, 55–129.
47. Zhou, L.; Gou, Y.; Hou, Z.; Were, P.; Hou, M.Z. Numerical modeling and investigation of fracture propagation with arbitrary orientation through fluid injection in tight gas reservoirs with combined XFEM and FVM. *Environ. Earth Sci.* **2015**, *73*, 5801–5813. [CrossRef]
48. Zhou, L.; Su, X.; Hou, Z.; Lu, Y.; Gou, Y. Numerical investigation of the hydromechanical response of a natural fracture during fluid injection using an efficient sequential coupling model. *Environ. Earth Sci.* **2016**, *75*, 1263. [CrossRef]

Disclaimer/Publisher's Note: The statements, opinions and data contained in all publications are solely those of the individual author(s) and contributor(s) and not of MDPI and/or the editor(s). MDPI and/or the editor(s) disclaim responsibility for any injury to people or property resulting from any ideas, methods, instructions or products referred to in the content.